Deformation behaviour of TiN and Ti–Al–N coatings at 295 to 573 K

Finn Giuliani[a], Constantin Ciurea[a], Vineet Bhakhri[a], Malcolm Werchota[b], Luc J. Vandeperre[a], Paul H. Mayrhofer[c,*]

[a] Centre for Advanced Structural Ceramics, Department of Materials, Imperial College London, UK
[b] Department of Metallurgy and Materials Testing, Montanuniversität Leoben, Austria
[c] Institute of Materials Science and Technology, TU Wien, Austria

ARTICLE INFO

ABSTRACT

Temperature-dependent nanoindentation testing was employed to investigate the deformation behaviour of magnetron sputtered (100) TiN and $Ti_{1-x}Al_xN$ (x = 0.34, 0.52, 0.62) coatings in the temperature range from 295 to 573 K. The maximum temperature is sufficiently below the deposition temperature of 773 K to guarantee for stable microstructure and stress state during testing. The TiN coating displayed the same hardness as bulk single crystal (SC) TiN_{bulk}. The addition of aluminium to TiN (to form single-phase face centred cubic structured $Ti_{1-x}Al_xN$ coatings) increased the room temperature hardness due to increased bond strength, lattice strain and higher activation energy for the dislocation slip. For coatings with a low aluminium content, $Ti_{0.66}Al_{0.34}N$, the decrease in hardness with temperature was similar to the TiN coating and SC-TiN_{bulk}. In contrast, the hardness of coatings with moderate, $Ti_{0.48}Al_{0.52}N$, and high, $Ti_{0.38}Al_{0.62}N$, aluminium contents varied little up to 573 K. Thus, the $Ti_{1-x}Al_xN$ matrix is mechanically more stable at elevated temperatures than its TiN relative, by providing a lower decrease in lattice resistance to the dislocation flow with increasing temperature. The findings suggest that the addition of Al to TiN (to form $Ti_{1-x}Al_xN$ solid solutions) not only improves the hardness but also leads to stable hardness with temperature, and emphasizes the importance of bonding states and chemical fluctuations, next to structure and morphology of the coatings that develop with changing the chemistry.

1. Introduction

Hard ceramic coatings are now routinely used in industrial applications particularly as surface protection coatings for cutting tools where wear, abrasion and erosion resistance characteristics are desirable [1–3]. During high speed machining processes, cutting tools are subjected to conditions such as high stresses, high temperatures, repeated impact and chemical attack. Metal-nitride, $Ti_{1-x}Al_xN$, coatings are used for high-temperature applications where good wear resistance and oxidation resistance are required [4]. The incorporation of aluminium in the cubic (NaCl-type, face centred cubic, fcc) TiN matrix results in a metastable solid solution (if not even thermodynamically instable). The superior tool performance of these fcc-$Ti_{1-x}Al_xN$ coatings is attributed to the isostructural decomposition, via spinodal decomposition, of this solid solution into coherent fcc-structured Al- and Ti-rich domains at elevated temperatures (~1073–1273 K) [5–8], leading to an increased hardness. Convincing theoretical and experimental research effort has been directed towards understanding the structural evolution and acquiring the micro-structural evidence for this effect [9–11]. Ab initio calculations based on density functional theory [9,12] have shown that the mixing enthalpy of fcc-TiN and fcc-AlN phases is very high, primarily due to unfavourable localization of Ti non-bonding electronic states. The high mixing enthalpy leads to the possibility of a negative second derivative of the free energy with respect to composition, and therefore results in spinodal decomposition [12].

In terms of microstructural evidence, Hörling et al. [5] interpreted the asymmetric broadening of the X-ray diffraction peaks of the cubic phase in a $Ti_{0.34}Al_{0.66}N$ coating annealed at 1173 K as spinodal decomposition. The Ti and Al segregation in $Ti_{0.34}Al_{0.66}N$/TiN multilayer coatings annealed at 1173 K was revealed by scanning transmission electron microscopy (TEM) elemental mapping, while high-resolution TEM showed Al-rich coherent domains, which were consistent with the spinodal-type decomposition of $Ti_{1-x}Al_xN$ towards fcc-TiN and fcc-AlN [6]. More recently, a 3D-atom probe tomography study by Rachbauer et al. [13] showed that at 1073 K an interconnected three dimensional network of Al-rich and Ti-rich domains in a single-phase $Ti_{0.46}Al_{0.54}N$ coating starts to develop; at 1623 K separated phases of TiN and AlN are formed. Through the extensive research on this material, a general

---

consensus has been drawn, that the increased tool performance stems from the formation of coherent fcc-structured Al- and Ti-rich domains at elevated temperatures [7].

Alongside microstructural characterization, several investigations have been carried out to investigate the mechanical behaviour of these coating materials. However, in most of these studies the coatings have only been tested at room temperature in either the as-deposited state or after heat-treatment [4,5,7,14–18]. Although this kind of approach, i.e. testing post-annealed specimens at ambient temperature is useful, it is advantageous to test materials as close to their service temperature as possible, where the intrinsic material properties are expected to change. Essential is to derive temperature-dependent deformation behaviours. This is particularly important in case of ceramics, where the materials with very high room-temperature hardness often show a considerable drop in hardness at low and moderately elevated temperatures due to the decrease in lattice resistance to the dislocation flow [19].

Here, the results from a systematic study conducted to obtain the mechanistic information on temperature-dependent deformation of TiN and $Ti_{1-x}Al_xN$ coatings using instrumented nano-indentation is reported. Initial experimental work was focussed on investigating the mechanical behaviour of a magnetron sputtered TiN coating with a (001) preferential orientation (grown on MgO substrate) and its results were compared with previously reported findings on bulk single crystal (001) facet TiN ($SC-TiN_{bulk}$) [19]. By investigating the same composition (TiN) in the same crystallographic orientation but with and without grain boundaries, the influence of grain boundaries and internal stresses on mechanical properties of the TiN system was determined. Furthermore, in order to investigate the influence of aluminium addition on the mechanical stability of the TiN system with temperature, magnetron sputtered $Ti_{1-x}Al_xN$ coatings with various contents of aluminium (x = 0.34, 0.52, 0.62) deposited under the same conditions were tested. These compositions were chosen based on previous studies, showing that all are single-phase fcc-structured, with $Ti_{0.38}Al_{0.62}N$ being close to the solubility limit before also hexagonal AlN-based phases crystallize during deposition [20]. The relatively low maximum testing temperature of 573 K, being clearly below the deposition temperature of 773 K, ensured the absence of any microstructural changes or recovery processes. These typically set in for annealing temperatures above the deposition temperature [3].

2. Experimental details and data analyses

Commercially procured (001) MgO single crystals (CrysTec GMBH, Germany) sized $10x10x1mm^3$ were used as a substrate for all the coatings investigated in this work. These substrates were first ultrasonically cleaned for 10 min in acetone and then with ethanol to remove any acetone residues. 2–3 μm thick TiN and $Ti_{1-x}Al_xN$ (x = 34, 52, 62 mol% AlN) coatings were deposited by reactive magnetron sputtering from a 6-in.-diameter Ti and a powder metallurgically prepared 6-in.-diameter $Ti_{0.5}Al_{0.5}$ target (both with 99.7% purity, Plansee Composite Materials GmbH) in an Ar + N_2 glow discharge using a laboratory-scale magnetically unbalanced DC magnetron sputtering system. Different Ti/Al ratios within the coatings were produced by adding Ti platelets (Ø5 × 2 mm^3, 99.99% purity) on the $Ti_{0.5}Al_{0.5}$ target race-track. All coatings were prepared with a substrate temperature of 773 K, a working gas pressure of 0.4 Pa, and a bias potential of −50 V. Further details on the deposition process are given in [20].

An Oxford Instruments INCA EDX (Energy Dispersive X-ray) unit, attached to a Jeol 6400 scanning electron microscope (SEM) was used to determine chemical composition of the deposited coatings. X-Ray diffraction (XRD) was used to characterise the crystallographic structure of the deposited coatings. X-ray diffractograms of the TiN and ternary $Ti_{1-x}Al_xN$ coatings were measured using a diffractometer (X'Pert PRO, The Netherlands) in the Bragg-Brentano configuration with Cu Kα radiation. A JEOL-2000 operating at 200 KeV was employed for bright-field (BF) imaging of TEM specimens prepared by Focused Ion Beam

(HELIOS NanoLab 600, USA) micro-machining and polishing.

Nanoindentation experiments were carried out to investigate the deformation behaviour of TiN and $Ti_{1-x}Al_xN$ coatings using the *Nanotest* (Micro Materials Ltd., Wrexham, UK) indentation platform. The system is equipped with a dual heater arrangement where a miniature heater is attached to the indenter tip and a separate heater is used to heat-up the specimen. This type of arrangement insures that specimen and indenter tip are at the same temperature during testing and therefore limits the introduction of artefacts due to heat flow in the indentation depth signal.

Indentation tests were carried out at 295, 373, 473, and 573 K, with a Berkovich indenter, under load-controlled condition. For all coatings, the indenter was loaded until it reached a maximum load of 50 mN at loading rates between 0.25 mN/s and 10 mN/s. The data were converted to strain rate following the procedure described previously by Bhakhri et al. [19]. The indenter was then unloaded at original loading rate and during unloading, thermal drift was estimated by monitoring the depth signal for 100 s at a minimal load (5 mN) value. Average thermal drift values of 0.05 nm/s at 295 K and 0.12 nm/s at 573 K were measured. The indentation data were corrected for this measured thermal drift of the system. Typical plastic depths corresponding to 50 mN load values ranged from 175 nm at 295 K to 225 nm at 573 K, which are all below 10% of the coating thickness. Hardness at temperatures from load-depth curves was calculated by adopting the procedure outlined by Oliver & Pharr [21]. Increasing plastic depth at 50 mN load with increasing temperature indicated that the coating hardness decreased with temperature.

A decrease in hardness with increasing temperature implies a decrease in resistance to dislocation flow during the deformation process. The relationship between the shear flow stress, strain rate and temperature can be described as follows:

The shear strain rate, $\dot{\gamma}$, produced by density, ρ_m, of mobile dislocations moving at an average velocity, $\bar{v}$, is given by the following phenomenological expression [22]:

$$\dot{\gamma} = \rho_m b \bar{v}, \tag{1}$$

where b is the magnitude of Burgers' vector of the dislocation. The velocity of the mobile dislocations through the lattice of a material is given by a kinetic equation:

$$\bar{v} = \vartheta b \left[\exp\left(-\frac{(\tau_p - \tau)V}{kT} \right) - \exp\left(-\frac{(\tau_p + \tau)V}{kT} \right) \right] \tag{2}$$

Where ϑ is the attempt frequency, τ_p is the Peierls' stress (stress required to make the dislocation move in the absence of thermal energy, i.e. at 0 K), τ is the applied shear-stress, V is the activation volume, k is Boltzmann's constant and T is the absolute temperature. If the applied mechanical work, τV, remains large to the available thermal energy, kT, then the second term in the square bracket of Eq.(2) becomes much lower than the first and can be ignored. Assuming the activation volume, V, can be treated constant over the tested temperature range, combining Eqs. (1) and (2) and solving for shear stress, results in the following relationship:

$$\tau = \tau_p + \frac{kT}{V} ln[\dot{\gamma}] - \frac{kT}{V} ln[\rho_m b^2 \vartheta] \tag{3}$$

From Eq. (3), a plot of shear stress, τ, versus natural logarithm of shear strain rate, $ln(\dot{\gamma})$, at a particular temperature, T, should result in a linear relationship with slope $\frac{kT}{V}$. Therefore, V can be determined from the obtained slope. Similarly, a plot of τ versus T at a particular strain-rate should yield a straight line whose intercept of τ-axis at 0 K provides an estimate of the Peierls stress (τ_p) for a pure material or shear flow stress required to move a dislocation on a slip plane at 0 K, τ_{0K}, for alloys or compositionally modulated systems such as $Ti_{1-x}Al_xN$ coatings in this work. Under these assumptions, the activation energy of the deformation process, Q, can then be calculated as $\tau_{p/0K}V$.

(a)

(b)
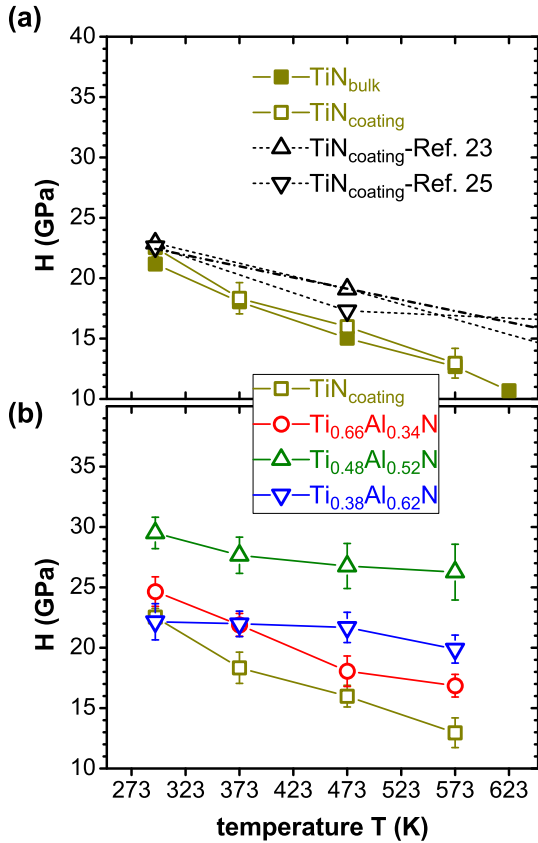
Fig. 1. Temperature-dependent mechanical property data; (a) The influence of temperature on hardness (H) of magnetron sputtered TiN (TiN$_{coating}$) and the SC-TiN$_{bulk}$ [19] determined by nanoindentation in this study. Also included are data on the influence of temperature on Vickers hardness (for comparative reasons simply converted into MPa by multiplying the presented VHN-50 g values given in kg/mm^2 with 9.81 m/s^2) of TiN magnetron sputtered coatings from Quinto et al. [23] and Jindal et al. [25]. (b) The influence of the Al addition on the temperature dependence of H for Ti$_{1-x}$Al$_x$N.

3. Results

3.1. Temperature and strain-rate dependence of hardness

The temperature variation of hardness of the magnetron sputtered TiN coating (TiN$_{coating}$) is shown in Fig. 1a, along with data from SC-TiN$_{bulk}$ [19] for comparison. For the TiN coating, the hardness dropped from 22.5 ± 0.7 GPa at 295 K to 13.0 ± 1.2 GPa at 573 K. Over the tested temperature range, 295 to 573 K, the TiN coating displayed a very similar hardness response to the SC-TiN$_{bulk}$, which exhibited a hardness drop from 21.2 ± 0.5 GPa at 295 K to 12.7 ± 0.4 GPa at 573 K. Also included in the figure are the data obtained by Quinto et al. [23], Quinto [24] and Jindal et al. [25] from Vickers indentation of magnetron sputter deposited TiN coatings, which show a similar trend of the hardness decrease with temperature.

The influence of Al substituting for Ti in the TiN lattice on the hardness of magnetron sputtered Ti$_{1-x}$Al$_x$N (with x = 0, 0.34, 0.52, 0.62) coatings, at various temperatures, is shown in Fig. 1b. The addition of Al to TiN resulted in higher room-temperature hardness, which is consistent with literature data [4,20,26,27]. The low Al content coating, Ti$_{0.66}$Al$_{0.34}$N, exhibited higher room temperature hardness than the TiN coating, but the hardness stability with the temperature for both these coatings followed a similar trend of a decrease in hardness by 8–9 GPa over 278 K. The intermediate Al composition, Ti$_{0.48}$Al$_{0.52}$N, showed not only a substantial increase in hardness at room temperature, but the hardness stability with temperature was also

improved compared to the TiN and Ti$_{0.66}$Al$_{0.34}$N coating. A hardness drop of only ~3 GPa, from 29.5 ± 1.3 GPa at 295 K to 26.3 ± 2.3 GPa at 573 K was observed. The Al-rich composition, Ti$_{0.38}$Al$_{0.62}$N exhibited also an improved hardness stability with temperature, although at considerably lower values, 22.2 ± 1.50 GPa at 295 K and 19.9 ± 1.2 GPa at 573 K. The reason for the lower hardness is in the more random-like growth orientation and different growth morphology (exhibiting a higher fraction of low density regions due to the significantly shorter columns), as discussed later. The different growth morphology and structure indicate that the chemical composition of this Ti$_{0.38}$Al$_{0.62}$N is rather close to the solubility limit for single-phase fcc-structured coatings, and that a hexagonal phase formation is looming (below the detection limit of the XRD used here), which is also discussed later.

The hardness and strain-rate data were used to determine the influence of aluminium addition on the kinetics of plastic deformation of the Ti$_{0.48}$Al$_{0.52}$N coating, and compared with the SC-TiN$_{bulk}$ [19] material. These materials exhibit the two extrema of mechanical behaviour; the Ti$_{0.48}$Al$_{0.52}$N coating showed both the highest hardness and good hardness stability with temperature, whereas SC-TiN$_{bulk}$ exhibited lowest hardness and poor hardness stability with temperature. The obtained hardness values were converted into uniaxial flow stress values using the analytical relationship between hardness, H, and yield stress, Y:

$$\frac{H}{Y} = \frac{2}{3}\left\{1 + \frac{3}{3-6\lambda}ln\left(\frac{(3+2\mu)[2\lambda(1-\zeta)-1]}{2\lambda\mu - 3\mu - 6\lambda} \times \frac{1}{\zeta}\right)\right\} \tag{4}$$

with $\zeta = \left[\frac{E}{E-2(1-v^2)H\tan\alpha}\right]$, $\lambda = (1-2v)\frac{Y}{E}$, $\mu = (1+v)$, where E is the Young modulus, v is the Poisson ratio and α is the equivalent semi angle of the indenter derived by Vandeperre et al. [28] by modifying the expanding cavity solution of Hill [29]. Uni-axial yield stress values were then converted into shear flow stress by dividing by 2, consistent with the Tresca yield criterion used in deriving the expanding cavity solution.

Fig. 2a shows the variation of τ with $\ln(\dot{\gamma})$ measured at 295 K for the Ti$_{0.48}$Al$_{0.52}$N coating and SC-TiN$_{bulk}$ [19], and the temperature dependence of τ at a particular strain-rate, $\dot{\gamma}$, for these materials is included in Fig. 2b. The activation volume determined from the slope of linear regression in Fig. 2a yielded 3.06·10^{-29} m^3 (1.14 × b^3) for the Ti$_{0.48}$Al$_{0.52}$N coating and 2.05·10^{-29} m^3 (0.76 × b^3) for SC-TiN$_{bulk}$ [19]. The magnitude of the Burgers vector b in ⟨110⟩ direction of the fcc-crystals (being the relevant slip direction, see chapter 3.2) is ~0.3 nm (i.e., half of the unit cells face-diagonal). These results are reasonable and consistent with literature values for various hard ceramics, such as SiC [19,30,31] and ZrB$_2$ [19]. The shear flow stress at 0 K, τ_{0K}, which can be treated as the Peierls stress, τ_p, for the Ti$_{0.48}$Al$_{0.52}$N coating (estimated from the intercept in Fig. 2b) is 7.2 GPa, compared to τ_p = 6.1 GPa for SC-TiN$_{bulk}$ [19].

The apparent activation energy, Q (= $\tau_{0K}V$), of the deformation process of the Ti$_{0.48}$Al$_{0.52}$N coating is about 1.37 eV (2.19·10^{-19} J), whereas Q (= τ_pV) for SC-TiN$_{bulk}$ is 0.77 eV (1.24·10^{-19} J) [19]. Consequently, the apparent activation energy Q of the deformation process of the Ti$_{0.48}$Al$_{0.52}$N coating is almost twice that of the Al-free SC-TiN$_{bulk}$. This increase in the apparent activation energy of deformation process is significant and presumably due to the presence of Al in the structure. Such an increase in the resistance to plastic flow is responsible for the significant improvement in hardness at 295 K for Ti$_{1-x}$Al$_x$N coatings, as well as good mechanical stability with temperature for the Ti$_{0.48}$Al$_{0.52}$N and Ti$_{0.38}$Al$_{0.62}$N coatings in particular.

The magnitude of apparent activation energy (~10^{-19} J) and activation volume (~1 b^3) of the deformation process for both materials, the Ti$_{0.48}$Al$_{0.52}$N coating and the SC-TiN$_{bulk}$ [19], indicate that lattice resistance controlled dislocation glide is the deformation rate controlling mechanism [22]. This is reasonable in case of ceramic materials, which have very high lattice resistance at low temperatures. Their high

(a)

(b)
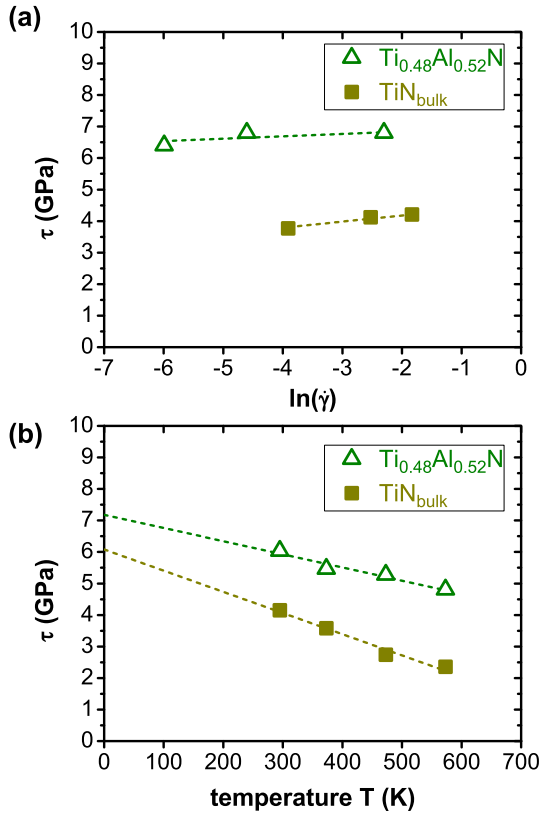
Fig. 2. (a) The variation of the shear flow stress, τ, with $\ln(\dot{\gamma})$ for TiN_{bulk} and $Ti_{0.48}Al_{0.52}N$ coating. The slope of the plot provides the activation volume (V). (b) Temperature dependence of τ for TiN_{bulk} and $Ti_{0.48}Al_{0.52}N$ coating. The extrapolation of the graph to 0 K gives the Peierls stress (τ_p). The strain rates used for obtaining the data presented in (a) are 0.0025, 0.01, and 0.1 s^{-1} for the $Ti_{0.48}Al_{0.52}N$ coating and 0.02, 0.08, and 0.16 s^{-1} for TiN_{bulk}.

lattice resistance dominantly controls the dislocation motion during plastic flow, regardless of the presence of other microstructural defects such as grain-boundaries.

3.2. Structural and crystallographic phase characterization

The drop in hardness with temperature as a result of decline in the lattice resistance to dislocation motion is translated in a change of intrinsic ease of plastic slip. Bright-field images taken at [001] zone axes from indents performed on TiN_{bulk} at 295 K and 623 K are presented in Fig. 3a and b, respectively. These clearly show that plastic flow during nanoindentation performed over the temperature range 295–623 K occurred primarily along {110} crystallographic planes. This is consistent with findings from compression tests carried at high temperature on fine-grained sintered TiN by Yamamoto et al. [32], showing that the primary slip system in TiN was {110}⟨110⟩.

The X-ray diffractograms provide information on the phase-content and texture. Fig. 4 shows that the TiN coating strongly followed the (200) orientation of the single crystal MgO substrate on which it was deposited. The main (200) XRD peak of the coating can clearly be identified at 2 theta = 42.61°, which is very close to the position corresponding to TiN (2 theta = 42.6°). Similarly, X-ray diffraction analysis revealed that the growth orientation of the low- and medium-Al containing $Ti_{1-x}Al_xN$ coatings was also (200), facilitated by the (200) MgO substrate. All three ternary coatings have a rocksalt NaCl type cubic crystal structure. Due to the substitution of titanium atoms with smaller aluminium ones and the changed bonding characteristics, the lattice parameter decreased, approaching the lattice parameter of MgO for $Ti_{0.38}Al_{0.62}N$ (therefore hidden behind that). This is in agreement
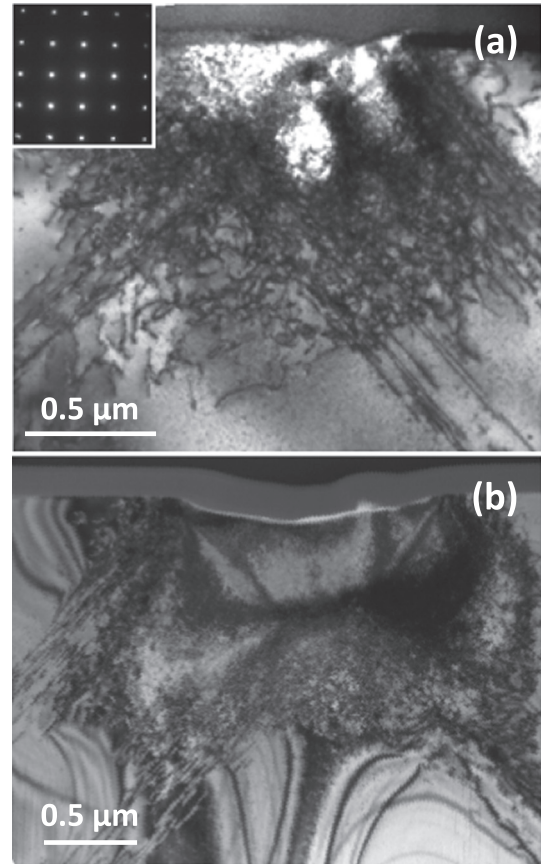
Fig. 3. Cross-section BF TEM images taken at [001] zone axis from 50 mN indents performed in the TiN_{bulk} at: (a) 295 K and (b) 623 K. The dominant plastic flow occurred along the {110} slip planes during indentation performed at various temperatures on bulk single crystal (001) TiN.
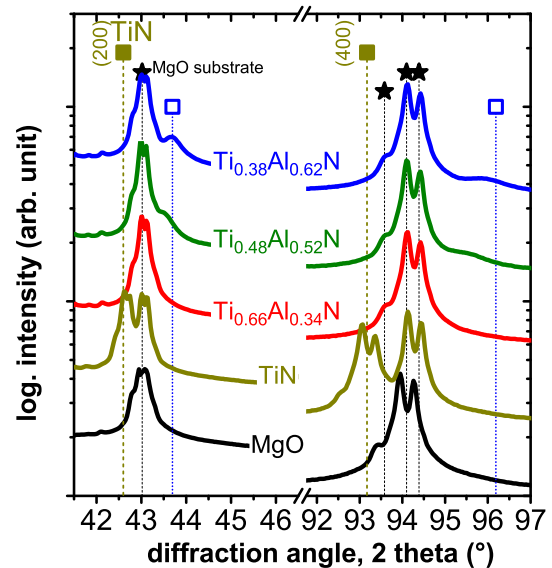
Fig. 4. X-ray pattern of TiN, $Ti_{0.66}Al_{0.34}N$, $Ti_{0.48}Al_{0.52}N$, and $Ti_{0.38}Al_{0.62}N$ coatings on a 200-oriented MgO substrate. The TiN coating has a strong (200) orientation allowing for the typical doublet. All films have a single-phase fcc lattice structure. Increasing the Al content led to the formation of fcc-$Ti_{1-x}Al_xN$ solid solutions with smaller lattice parameters. The empty square symbol indicates the 2 theta position for a lattice parameter of 4.14 Å (the fcc-TiN (indicated with a solid square) has 4.24 Å). The asterisks represent the peaks attributed to the single-crystal MgO substrate.

with ab initio calculations and experiments, which highlight that the lattice parameter of fcc-$Ti_{1-x}Al_xN$ decreases from 4.24 to 4.21 to 4.18 to 4.16 Å with increasing Al content (x) from 0 to 0.34 to 0.52 to 0.62, respectively [33]. Hence, the MgO peaks are indeed expected to hide the XRD peaks for fcc-$Ti_{0.66}Al_{0.34}N$, in agreement to their almost perfect match in lattice parameters of 4.212 and 4.21 Å, respectively. The shift of the XRD peaks towards larger diffraction angles (smaller lattice parameters) with increasing Al content is shown in Fig. 4 by the (200) and (400) peak position of the fcc cell having a lattice parameter of 4.14 Å (empty square symbols). The fcc-TiN (indicated with solid squares) has 4.24 Å.

For $Ti_{0.38}Al_{0.62}N$, a distinct XRD peak on the right side close to the major MgO peak (at ~43.5°) can be identified, whereas for $Ti_{0.48}Al_{0.52}N$ only a right-hand shoulder formation is detectable. Furthermore, these two coatings exhibit also additional 111- and 311-oriented crystals (with higher XRD peak intensities and even 220-oriented crystals for the higher-Al containing coating). These orientations are not shown in Fig. 4 as we focused on the (200) and (400) XRD peaks, being dominating for the fcc-$Ti_{1-x}Al_xN$ coatings with x = 0, 0.34, and 0.52.

The TEM micrograph, Fig. 5a, shows that the TiN coating exhibits a polycrystalline structure with columnar morphology. The first stages of deposition were epitaxial to the MgO substrate, up to an approximate thickness of 300 nm, above which a columnar structure develops. Due to the relatively high energy of deposition (−50 V bias, see experimental), sufficient residual ion damage was produced to disrupt the columnar structure and continuously nucleate new grains [34–37]. Similarly prepared TiN, $Ti_{0.48}Al_{0.52}N$, and $Ti_{0.38}Al_{0.62}N$ coatings (but on Si substrates and with −60 V bias) exhibit compressive stresses of −1.4, −1.4, and −0.9 GPa, respectively [20].

Fig. 5b, c and d show bright-field cross-sectional TEM images for the ternary $Ti_{1-x}Al_xN$ coatings with x = 0.34, 0.52 and 0.62, respectively, having columnar structures. The selected area electron diffraction (SAED) investigations (not shown here) for $Ti_{0.66}Al_{0.34}N$ show a rock-salt NaCl type cubic crystal structure and an epitaxial growth up to 300 nm film-thickness after which, in agreement to the observations for

TiN, a columnar structure develops. With further addition of aluminium, the columnar structure of the coatings is less well defined, demonstrating a loss in texture. This is also observed during XRD studies (as mentioned above), indicating also the formation of 111- and 311-oriented crystals for the $Ti_{0.48}Al_{0.52}N$ coating and additional 220-oriented crystals for the $Ti_{0.38}Al_{0.62}N$ coating. The latter, actually exhibits a rather equiaxed nanostructure, Fig. 5d.

Higher magnification imaging, inset Fig. 5a, revealed lower-density regions (possible voids and bubbles of trapped Ar and N_2 gases [38]) gathered along the column boundaries in the TiN coating. These lower-density regions observed can be attributed to the effect of atomic shadowing during the process of texture evolution via competitive growth [34,37]. Insets of Fig. 5b, c and d show the influence of Al addition on such type of lower-density regions in ternary $Ti_{1-x}Al_xN$ coatings. The substitution of 34 and 52% Ti within TiN by Al, i.e. $Ti_{0.66}Al_{0.34}N$ and $Ti_{0.48}Al_{0.52}N$, did not change the amount of lower-density regions (insets Fig. 5b and c), which were mainly detected as fine lines along grain boundaries, similar to the TiN coating (inset Fig. 5a). A further addition of Al, $Ti_{0.38}Al_{0.62}N$, results in significantly shorter columns (almost equiaxed nanostructure, as mentioned above). Thus, providing a higher fraction of preferred sites with regions of lower density, which is evident from inset Fig. 5d. Consequently, this coating contains a higher fraction of lower-density regions, explaining their lower hardness. These lower-density regions, which for $Ti_{0.38}Al_{0.62}N$ are also intra-columnar, are also indications for the looming formation of hexagonal phases, as the chemical composition is rather close to the solubility limit for obtaining single-phase fcc-structured coatings [20]. Hexagonal AlN has a considerably lower density than fcc-AlN [33,39].

4. Discussion

The first objective of this work is to investigate the influence of microstructure, i.e. the presence or absence of grain boundaries, on the mechanical behaviour of TiN at different temperatures. As shown in Fig. 1a, for the tested temperatures (295 to 573 K) the TiN coating displayed similar hardness response to SC-TiN_{bulk} [19]. Thus, the
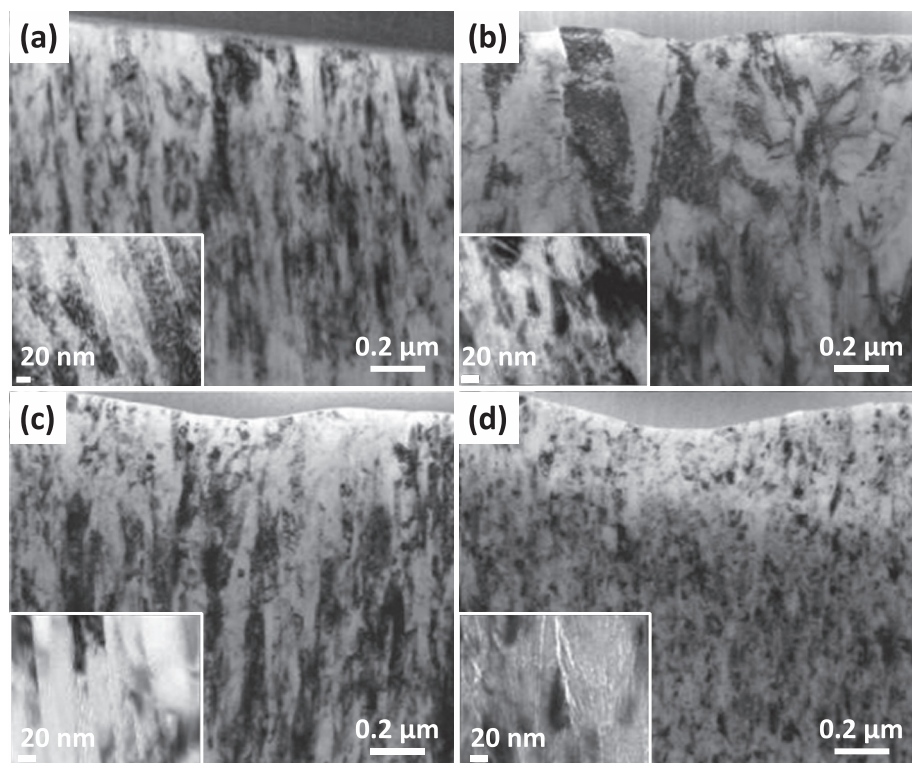
Fig. 5. Cross-section BF TEM images from magnetron sputtered coatings showing the change in columnar structure with the Al content; (a) TiN, (b) $Ti_{0.66}Al_{0.34}N$, (c) $Ti_{0.48}Al_{0.52}N$, (d) $Ti_{0.38}Al_{0.62}N$. The higher resolution images depicting the influence of Al addition on the column boundary morphology of respective coatings are included in insets.

deformation kinetics analyses of the TiN system (Section 3.1) revealed that the operative deformation-rate controlling mechanism over the tested temperature range is "lattice resistance controlled" dislocation glide. The presence of grain-boundaries in TiN has either little effect on the deformation behaviour of these materials or any effect is balanced by the small amounts of lower-density regions in the film. Important to mention here is, that the maximum testing temperature of 573 K is sufficiently below the deposition temperature of 773 K to ensured that no microstructural changes or recovery processes (where built-in structural defects would rearrange towards lower energy configurations) set in [3]. This allows to derive temperature-dependent deformation mechanisms that are not superimposed by microstructural changes and/or stress changes (except those induced by the differential thermal expansion between coating and substrate, which are relatively small).

A strained (distorted) TiN type lattice is formed when Ti is substituted with Al, due to the difference between their atomic sizes (Al = 1.43 Å and Ti = 1.47 Å) and the lengths of the atomic bonding (Ti−N bond > Al−N bond [40]). In addition, the bond strength has been shown to increase due to an increase in covalence component of the atomic bonding, as Al has a closer electronegativity to N than Ti [41]. AlN, being a semiconductor has no metallic bonding in contrast to TiN. The improved room-temperature hardness of the $Ti_{0.66}Al_{0.34}N$ coating compared to TiN coating can be explained by the increase in both the lattice strain and strength of the atomic bonding and is consistent with literature data [41]. However, the rate of hardness drop with temperature for this coating remained similar to the TiN coating. An increase in Al concentration to 52%, $Ti_{0.48}Al_{0.52}N$, resulted in a significantly higher hardness, and more importantly, improved mechanical stability with temperature. The higher hardness can be attributed to further increase in the bond strength and the lattice strain. Atom probe tomography on sputtered single-phase fcc-$Ti_{0.46}Al_{0.54}N$ coatings (using the same deposition temperature and same powder metallurgically prepared $Ti_{0.5}Al_{0.5}$ target) clearly showed that a 3D interconnected network of Ti-rich and Al-rich domains already exists in the as-deposited state of the film [13]. The formation of these domains due to chemical fluctuations is based on the high driving force for spinodal decomposition present in these coatings, which is maximum for x ~0.65 [12,33]. Adibi et al. [42] showed that for a similar chemical composition of fcc-$Ti_{0.5}Al_{0.5}N$, surface diffusion driven spinodal decomposition leads to Al-rich and Ti-rich layer formation during epitaxial growth on MgO 001 at 570 °C. These layered structures vary by ~0.2 Å in lattice parameters between Ti-rich (~4.25 Å) and Al-rich (4.05 Å) layers. This lattice mismatch has to be accommodated by distortion of the lattices in order to form coherent grain boundaries between two crystallographic domains, leading to a coherent strained lattice structure. This has been proven for epitaxial layers [42] as well as polycrystalline $Ti_{0.46}Al_{0.54}N$ [43]. Therefore, the improved hardness stability with temperature for the $Ti_{0.48}Al_{0.52}N$ coating is attributed to the presence of such chemical fluctuations within the solid solutions. This results in a better mechanical stability with temperature. Therefore, we suggest that for good hardness stability with temperature of such ternary coatings the presence of corresponding fluctuations in bond length and strength is required.

A further addition of Al results in more or larger such chemical fluctuations. The maximum is of course at a chemical composition of x = 0.5, which provides the necessary condition for maximum interference, as highlighted in [44]. Nevertheless, an Al content of x = 0.62 provides a higher chemical driving force spinodal decomposition than an Al content of 0.52. Hence, we envision, that the higher Al-containing coating provides actually a higher chemical fluctuation leading to higher coherency strains. This is supported by various experimental investigations showing that $Ti_{0.34}Al_{0.66}N$ coatings spinodally decompose earlier and faster than $Ti_{0.5}Al_{0.5}N$ [10]. Therefore, our $Ti_{0.38}Al_{0.62}N$ coatings provide an even better hardness stability with temperature than $Ti_{0.48}Al_{0.52}N$ coatings. However, the actual hardness values of $Ti_{0.38}Al_{0.62}N$ dropped considerably compared to $Ti_{0.48}Al_{0.52}N$. This mighty also be a consequence of the higher chemical driving force for decomposition, leading to the onset-formation of hexagonal phases. Detailed TEM investigations suggest that the higher fraction (as compared to the other films) of inter- and intra-columnar lower-density regions (Fig. 5d) are responsible for the lower hardness. These low-density regions indicate the looming formation of hexagonal phases (which are not crystalline and therefore not observed during XRD and SAED).

5. Conclusions

Instrumented nanoindentation testing was employed to investigate the difference between the deformation behaviour of TiN and $Ti_{1-x}Al_xN$ (x = 0.34, 0.52, 0.62) coatings at 295 K to 573 K. The maximum testing temperature is sufficiently below the deposition temperature of 773 K to ensure the absence of any microstructural changes and recovery effects in the coatings during testing.

The temperature-dependent nanoindentation showed that the hardness of TiN coating and SC-TiN_{bulk} drop with temperature by around 9 GPa over the temperature range tested. The similarity in hardness values and temperature dependence for these two materials indicate that the presence of grain-boundaries in our TiN coating only has a minor influence on the dislocation flow behaviour in the material, at moderately elevated temperatures. Consequently, the operative deformation-rate controlling mechanism over the tested temperature range is basically "lattice resistance controlled" dislocation glide.

The addition of aluminium to form $Ti_{1-x}Al_xN$ coatings increased the room temperature hardness due to increased bond strength, lattice strain and increased activation energy for the dislocation slip in the material at 295 K to 573 K. The reduction in hardness when 62% of Ti was substituted by Al is due to the increased formation of lower-density regions, indicating the looming formation of hexagonal phases.

The temperature dependence of hardness of the low aluminium content coating, $Ti_{0.66}Al_{0.34}N$, followed a decreasing trend similar to the trends observed for the TiN coating and SC-TiN_{bulk}. However, the hardness of the coatings with moderate, $Ti_{0.48}Al_{0.52}N$, and high, $Ti_{0.38}Al_{0.62}N$, aluminium compositions remained stable in the measured temperature range. The stable hardness over temperature is based on the presence of chemical fluctuations in the $Ti_{1-x}Al_xN$ matrix, resulting in strained lattices rendering mechanical stability to $Ti_{0.48}Al_{0.52}N$ and $Ti_{0.38}Al_{0.62}N$ coatings at elevated temperatures.

Acknowledgments

References

[1] H. Holleck, V. Schier, Multilayer PVD coatings for wear protection, Surf. Coat. Technol. 76–77 (1995) 328–336.

[2] A.A. Voevodin, J.P. O'Neill, J.S. Zabinski, Nanocomposite tribological coatings for aerospace applications, Surf. Coat. Technol. 116–119 (1999) 36–45.

[3] P.H. Mayrhofer, C. Mitterer, L. Hultman, H. Clemens, Microstructural design of hard coatings, Prog. Mater. Sci. 51 (8) (2006) 1032–1114.

[4] A. Hörling, L. Hultman, M. Oden, J. Sjolen, L. Karlsson, Mechanical properties and machining performance of TiAlN-coated cutting tools, Surf. Coat. Technol. 191 (2–3) (2005) 384–392.

[5] A. Hörling, L. Hultman, M. Odén, J. Sjölén, L. Karlsson, Thermal stability of arc evaporated high aluminum-content $Ti_{1-x}Al_xN$ thin films, J. Vac. Sci. Technol. A 20 (5) (2002) 1815–1823.

[6] A. Knutsson, M.P. Johansson, P.O.Å. Persson, L. Hultman, M. Odén, Thermal decomposition products in arc evaporated TiAlN/TiN multilayers, Appl. Phys. Lett. 93 (14) (2008) 14–16.

[7] P.H. Mayrhofer, A. Hörling, L. Karlsson, J. Sjölén, T. Larsson, C. Mitterer, L. Hultman, Self-organized nanostructures in the Ti–Al–N system, Appl. Phys. Lett. 83 (10) (2003) 2049.

[8] L. Chen, Y. Du, P.H. Mayrhofer, S.Q. Wang, J. Li, The influence of age-hardening on turning and milling performance of Ti-Al-N coated inserts, Surf. Coat. Technol. 202

(21) (2008) 5158–5161.

[9] B. Alling, A. Ruban, A. Karimi, O. Peil, S. Simak, L. Hultman, I. Abrikosov, Mixing and decomposition thermodynamics of c-Ti$_{1-x}$Al$_x$N from first-principles calculations, Phys. Rev. B 75 (4) (2007) 1–13.

[10] P.H. Mayrhofer, L. Hultman, J.M. Schneider, P. Staron, H. Clemens, Spinodal decomposition of cubic Ti$_{1-x}$Al$_x$N: Comparison between experiments and modeling, Int. J. Mater. Res. 98 (11) (2007) 1054–1059.

[11] J.L. Endrino, C. Rhammar, A. Gutiérrez, R. Gago, D. Horwat, L. Soriano, G. Fox-Rabinovich, D. Martín, Y. Marero, J. Guo, J.E. Rubensson, J. Andersson, Spectral evidence of spinodal decomposition, phase transformation and molecular nitrogen formation in supersaturated TiAlN films upon annealing, Acta Mater. 59 (16) (2011) 6287–6296.

[12] P.H. Mayrhofer, D. Music, J.M. Schneider, Ab initio calculated binodal and spinodal of cubic Ti$_{1-x}$Al$_x$N, Appl. Phys. Lett. 88 (7) (2006) 071922.

[13] R. Rachbauer, E. Stergar, S. Massl, M. Moser, P.H. Mayrhofer, Three-dimensional atom probe investigations of Ti-Al-N thin films, Scr. Mater. 61 (7) (2009) 725–728.

[14] L. Karlsson, A. Hörling, M.P. Johansson, L. Hultman, G. Ramanath, The influence of thermal annealing on residual stresses and mechanical properties of arc-evaporated TiC$_x$N$_{1-x}$ (x=0, 0.15 and 0.45) thin films, Acta Mater. 50 (20) (2002) 5103–5114.

[15] P.H. Mayrhofer, C. Mitterer, H. Clemens, Thermal stability of nanostructured TiN-TiB$_2$ thin films, Mater. Res. 854 (2005) 1–6.

[16] L. Hultman, Thermal stability of nitride thin films, Vacuum 57 (1) (2000) 1–30.

[17] P.H. Mayrhofer, G. Tischler, C. Mitterer, Microstructure and mechanical/thermal properties of Cr-N coatings deposited by reactive unbalanced magnetron sputtering, Surf. Coat. Technol. 142–144 (2001) 78–84.

[18] P.H. Mayrhofer, C. Mitterer, J.G. Wen, J.E. Greene, I. Petrov, Self-organized nanocolumnar structure in superhard TiB$_2$ thin films, Appl. Phys. Lett. 86 (13) (2005) 131909.

[19] V. Bhakhri, J. Wang, N. Ur-rehman, C. Ciurea, F. Giuliani, L.J. Vandeperre, Instrumented nanoindentation investigation into the mechanical behavior of ceramics at moderately elevated temperatures, J. Mater. Res. 27 (1) (2012) 65–75.

[20] L. Chen, J. Paulitsch, Y. Du, P.H. Mayrhofer, Thermal stability and oxidation resistance of Ti-Al-N coatings, Surf. Coat. Technol. 206 (11–12) (2012) 2954–2960.

[21] W.C. Oliver, G.M. Pharr, An improved technique for determining hardness and elastic modulus using load and displacement sensing indentation experiments, J. Mater. Res. 7 (06) (1992) 1564–1583.

[22] H.J. Frost, M.F. Ashby, Deformation-Mechanism Maps: The Plasticity and Creep of Metals and Ceramics, 1st ed., Oxford, New York; Sydney: Pergamon, 1982.

[23] D.T. Quinto, G.J. Wolfe, P.C. Jindal, High temperature microhardness of hard coatings produced by physical and chemical vapor deposition, Thin Solid Films 153 (1–3) (1987) 19–36.

[24] D.T. Quinto, Mechanical property and structure relationships in hard coatings for cutting tools, J. Vac. Sci. Technol. A 6 (3) (1988) 2149–2157.

[25] P.C. Jindal, A.T. Santhanam, U. Schleinkofer, A.F. Shuster, Performance of PVD TiN, TiCN, and TiAlN coated cemented carbide tools in turning, Int. J. Refract. Met. Hard Mater. 17 (1) (1999) 163–170.

[26] A. Kimura, H. Hasegawa, K. Yamada, T. Suzuki, Effects of Al content on hardness, lattice parameter and microstructure of Ti$_{1-x}$Al$_x$N films, Surf. Coat. Technol. 120–121 (1999) 438–441.

[27] Y. Tanaka, T.M. Gür, M. Kelly, S.B. Hagstrom, T. Ikeda, Properties of (Ti$_{1-x}$Al$_x$)N coatings for cutting tools prepared by the cathodic arc ion plating method, J. Vac. Sci. Technol. A 1749 (1992) 1749–1756.

[28] L.J. Vandeperre, F. Giuliani, W.J. Clegg, Effect of elastic surface deformation on the relation between hardness and yield strength, J. Mater. Res. 19 (12) (2004) 3704–3714.

[29] R. Hill, The Mathematical Theory of Plasticity, Clarendon Press, 1998.

[30] S. Fujita, K. Maeda, S. Hyodo, Dislocation glide motion in 6H SiC single crystals subjected to high-temperature deformation, Philos. Mag. A 55 (2) (1987) 203–215.

[31] P. Pirouz, J.L. Demenet, M.H. Hong, On transition temperatures in the plasticity and fracture of semiconductors, Philos. Mag. A Phys. Condens. Matter Struct. Defects Mech. Prop. 81 (5) (2001) 1207–1227.

[32] R. Yamamoto, S. Murakami, K. Maruyama, High-temperature mechanical properties of hot-pressed TiN with fine grain size, J. Mater. Sci. 33 (8) (1998) 2047–2052.

[33] P.H. Mayrhofer, D. Music, J.M. Schneider, Influence of the Al distribution on the structure, elastic properties, and phase stability of supersaturated Ti$_{1-x}$Al$_x$N, J. Appl. Phys. 100 (9) (2006) 094906.

[34] L. Hultman, G. Håkansson, U. Wahlström, J.E. Sundgren, I. Petrov, F. Adibi, J.E. Greene, Transmission electron microscopy studies of microstructural evolution, defect structure, and phase transitions in polycrystalline and epitaxial Ti$_{1-x}$Al$_x$N and TiN films grown by reactive magnetron sputter deposition, Thin Solid Films 205 (2) (1991) 153–164.

[35] I. Petrov, L. Hultman, U. Helmersson, J.-E. Sundgren, J.E. Greene, Microstructure modification of TiN by ion bombardment during reactive sputter deposition, Thin Solid Films 169 (2) (1989) 299–314.

[36] I. Petrov, P.B. Barna, L. Hultman, J.E. Greene, Microstructural evolution during film growth, J. Vac. Sci. Technol. A Vacuum Surf. Film 21 (5) (2003) S117–S128.

[37] K.-H. Muller, Ion-beam-induced epitaxial vapor-phase growth: a molecular-dynamical study, Phys. Rev. B 35 (15) (1987) 7906–7913.

[38] L. Hultman, Transmission electron microscopy of metastable materials, Key Eng. Mater. 103 (1995) 181–194.

[39] Q. Xia, H. Xia, A.L. Ruoff, Pressure-induced rocksalt phase of aluminum nitride: a metastable structure at ambient condition, J. Appl. Phys. 73 (12) (1993) 8198–8200.

[40] A. Madan, I.W. Kim, S.C. Cheng, P. Yashar, V.P. Dravid, S.A. Barnett, Stabilization of cubic AlN in epitaxial AlN/TiN superlattices, Phys. Rev. Lett. 78 (9) (1997) 1743–1746.

[41] M. Zhou, Y. Makino, M. Nose, K. Nogi, Phase transition and properties of Ti-Al-N thin films prepared by r.f.-plasma assisted magnetron sputtering, Thin Solid Films 339 (1–2) (1999) 203–208.

[42] F. Adibi, I. Petrov, L. Hultman, U. Wahlström, T. Shimizu, D. McIntyre, J.E. Greene, J.-E. Sundgren, Defect structure and phase transitions in epitaxial metastable cubic Ti0.5Al0.5N alloys grown on MgO(001) by ultra-high-vacuum magnetron sputter deposition, J. Appl. Phys. 69 (9) (1991) 6437.

[43] R. Rachbauer, S. Massl, E. Stergar, D. Holec, D. Kiener, J. Keckes, J. Patscheider, M. Stiefel, H. Leitner, P.H. Mayrhofer, Decomposition pathways in age hardening of Ti-Al-N films, J. Appl. Phys. 110 (2) (2011) 023515.

[44] P.H. Mayrhofer, F.D. Fischer, H.J. Böhm, C. Mitterer, J.M. Schneider, Energetic balance and kinetics for the decomposition of supersaturated Ti$_{1-x}$Al$_x$N, Acta Mater. 55 (4) (2007) 1441–1446.